From 3D to 2D Co and Ni Oxyhydroxide Catalysts: Elucidation of the Active Site and Influence of Doping on the Oxygen Evolution Activity

Tripkovic, Vladimir; Hansen, Heine Anton; Vegge, Tejs

Published in:
A C S Catalysis

Link to article, DOI:
10.1021/acscatal.7b02712

Publication date:
2017

Document Version
Peer reviewed version

From 3D to 2D Co and Ni oxyhydroxide catalysts – elucidation of the active site and influence of doping on the oxygen evolution activity

Vladimir Tripkovic[1*], Heine Anton Hansen[1], Tejs Vegge[1]

[1] Department of Energy Conversion and Storage, Technical University of Denmark, DK-2800 Kgs. Lyngby, Denmark.

[*]Vladimir Tripkovic: tripce@gmail.com,

Heine Anton Hansen: heih@dtu.dk

Tejs Vegge: teve@dtu.dk

Layered oxyhydroxides (ox-hy) of Ni and Co are among the most active catalysts for oxygen evolution in alkaline media. Their activities can be further tuned by delamination into single-layer oxide sheets, or by means of doping. The active site for the reaction and how doping and delamination promote the intrinsic activity, however, remain elusive. To shed light on these open questions we have undertaken a systematic analysis of the stability, catalytic activity and electronic conductivity of Ni and Co ox-hys ranging from bulk (3D) to single-layer (2D) catalysts. In both cases, we investigate the role of terrace and edge sites and use stability, catalytic activity and electronic conductivity as evaluation criteria to pinpoint the best catalysts. We arrive at several important conclusions: the ox-hy surface is fully oxidized at oxygen evolution conditions, bulk terraces are ostensibly the most active sites and Ni ox-hy sheets are more electronically conductive compared to their Co equivalents. Furthermore, we examine 25 different doped Co and Ni ox-hy nanosheets (V, Cr, Mn, Fe, Co/Ni, Cu, Ru, Rh, Pd, Ir, Pt, Ag, Al, Ga, In, Sn, Pb, Bi, Mg, Sc, Y, Ti, Nb, Zn and Cd) to further tailor the catalytic performance. We establish the dependence of the electronic conductivity and activity on potential and find that it is more energetically favorable to dope Ni than Co ox-hys, with first row transition and noble metals being the most stable dopants. Finally, we extend the analysis to include bulk terminations and reveal that most dopants, which are stable in the nanosheets, have a large propensity to segregate to the surface of bulk materials, and those that are less prone to segregation (Fe or Cr) are not electronically conductive in the bulk. Overall, we identify Rh-doped Ni ox-hy to be the best catalyst material.

Keywords: Oxygen evolution reaction, density functional theory, doping, Ni oxide, Co oxide.

1. Introduction

To accommodate the intermittency of electricity produced from renewable sources, electrical energy must be stored in an energy carrier while the production is high and/or demand low, and converted back to electricity when conditions are reversed. Energy production and storage in the form of, e.g. hydrogen, hydrocarbons and batteries could, in principle, be used to power the entire energy grid if there were cost-effective ways to interchange between chemical and electrical energy.

For running water electrolyzer cells and for charging aqueous metal-air batteries, the main bottleneck is the oxygen evolution reaction (OER) at the anode.[1,2] Further development of these technologies requires increasing anode efficiencies by finding/designing more active catalysts. In acid, the precious metal oxides RuO_2 and IrO_2 are the best oxygen evolving electrocatalysts.[3–10] They are conductive, feature reasonably low overpotentials for the oxygen evolution reaction (OER) and can withstand highly oxidizing conditions under which the cells operate. However, their moderate activities coupled with high catalyst costs do not make electrolyzers and aqueous metal-air batteries competing products on the market. Switching to alternative alkaline electrolytes offers a solution to this problem, since the alkaline media is much less corrosive to earth abundant oxides, and thus permits a significantly broader selection of potential catalysts. First raw transition metal oxides are of particular interest because of their abundance and low cost. Furthermore, they possess rich chemistries, accept different oxidation states, and can be easily tuned for targeted applications.[3,11–13] Ni and Co oxides belong to this class. They are stable OER catalysts in the pH range from neutral to alkaline,[6] with activities on par with those for IrO_2 and RuO_2.[6,14–16] The performance of first row transition metals is further enhanced by increasing the population of active surface sites,[17,18] through nanostructuring[13,15,19,20] or dopant incorporation.[15,21–23]

A general way to produce ox-hys is from layered double hydroxides (LDH), which are typically synthesized *via* co-precipitation of precursor salts at a fixed pH.[24–26] Ni and Co LDHs are composed of alternating positively charged layers of hydroxide sheets and charge balancing anions (OH^-, Cl^-, Br^-, NO_3^-, CO_3^{2-} etc.) intercalated between the sheets.[15,25,27–29] Intercalated ions are readily exchanged for other types of anions present in the solution.[15,25,30] The inter-layer separation can be controlled by the size of the intercalated ion. Large ions increase the interlayer spacing, eventually leading to chemical exfoliation into single layer nanosheets (NS) or nanoplatelets.[15,19,30,31] The delamination increases the number of accessible active sites, resulting in an activity increase. Furthermore, it has been shown that the activity per site, measured by the turnover frequency, increases as well, suggesting that some beneficial electronic effect is taking place during delamination.[15] As mentioned, an alternative approach to enhance the performance is *via* chemical doping. From experimental analyses, Fe is seemingly the best doping element because the Fe doped Ni ox-hy has demonstrated unprecedented activity for the OER in alkaline media.[26,32–39] This result has been interpreted through synergistic effect of Fe and Ni, where the role of Fe is to provide more active sites for oxygen evolution and the role of Ni to provide electron conductive framework.[33,40] Recent experiments on Fe_2O_3 thin films have shown that Fe_2O_3 is intrinsically more

active than Co[41] and Ni ox-hys,[40,42] and that the true limiting factor is the poor electronic conductivity of bulk Fe_2O_3. Ni doped Fe_3O_4 is another good OER catalyst, which further substantiates the synergistic interplay between Ni and Fe.[43–45] Fe has a high propensity to incorporate spontaneously into Co and Ni LDH,[40,46,47] therefore the electrolyte solutions need to be purified from any traces of Fe (ppm concentrations in solution are sufficient to contaminate the catalyst) prior to any experimental analysis.[40,46] Earlier reports on the high activities of different doped Ni ox-hy catalysts were likely affected by Fe contamination.[40–42]

It is still unclear how nanostructuring and doping influences the OER performance, i.e. whether it is through improved electronic conduction, catalytic activity or perhaps through a combined effect. It is hypothesized that the edge sites are the active sites for OER, and the reason why 2D outperform 3D materials was ascribed to a large edge-to-surface ratio of the former.[15] To reveal the nature of the active sites, we have undertaken a systematic analysis of the activity and electronic conductivity of terrace and edge sites for the OER going from 3D bulk oxides to 2D NS.

The paper is divided into two parts. In the first part, we present results on pure 3D and 2D Co/Ni ox-hy terraces and edges. In the second part, we evaluate the performance of doped ox-hys using 25 different metals at a fixed concentration of ¼ mono layer (ML). By using three fundamental material properties: structural stability, catalytic activity and electron conductivity as selection criteria, we systematically reduce the number of candidates from an initial pool of 50 to only a few with optimal properties. Throughout the paper and especially in the theory section we critically discuss some of necessary approximations used ubiquitously at this level of theory.

2. Method

Total energies are calculated using Density Functional Theory (DFT) calculations with the RPBE exchange-correlation functional as implemented in the grid-based projector-augmented wave (GPAW) code.[48] For treating electron correlations we apply the Hubbard U correction on partially filled transition metal *d* electron levels using the implementation by Dudarev.[49] The code is integrated with the python-based Atomic Simulation Environment (ASE) package used to specify atomic positions and parameters for the GPAW calculator.[50] For bulk calculations, we use a very fine grid with the 0.12 Å grid spacing to get converged results for lattice constants and formation energies. For surface calculations, we use a coarser grid with the 0.18 Å grid spacing, which is sufficiently accurate for getting good estimates of adsorption energies and reaction overpotentials.

We use spin-polarized calculations to account for the ferromagnetic (FM) or antiferromagnetic (AFM) ordering in the bulk materials. The different magnetic arrangement has little effect on the total energy; e.g. we find an energy difference of 25 meV for bulk NiOOH. The occupation of one-electron states is calculated at an electronic temperature of k_BT = 0.1 eV, and then extrapolated to k_BT = 0 K. The only exception is the (0001) surface of Ni ox-hy, where we employed k_BT = 0.3 eV instead. This electronic temperature produces slightly larger errors (for a single NiO_2 layer, changing k_BT from 0.1 to 0.3 eV decreased the reaction overpotential from 0.60 to 0.54 eV), but was necessary to achieve convergence. The U values for Co and Ni were computed by fitting reaction enthalpies of following reactions to experimental values:

$$CoO + H_2O = CoOOH + ½\ H_2 \quad (1)$$

$$NiO + H_2O = NiOOH + ½\ H_2. \quad (2)$$

We computed U = 3.2 and 4.0 eV for reaction (1) and (2), respectively. Applying the U correction weakens the binding energies of reaction intermediates, and it does so more for O than OH. The weakening increases the reaction overpotential in cases where oxidation of OH to O is the Potential Determining Step (PDS), i.e. the step with the highest Gibbs free energy.[51] The reaction overpotential increases by 0.22 V going from U = 0 to U = 4 eV for the CoO_2 NS in concordance with results on Co_3O_4 and CoOOH.[51] However, for the NiO_2 NS the opposite effect is observed, i.e. the overpotential decreases from 0.98 to 0.60 V for changing the U value from 0 to 3.2 eV. The large downshift in the overpotential with U might explain why NiOOH and other Ni containing catalysts feature low calculated overpotentials in atomic-scale calculations.[22,52]

It is well-known that applying the U correction gives a much better description of the electronic structure in strongly correlated systems. However, it is not given that fitting the U value to reaction energies will give good estimates of the binding energies and reaction overpotentials. A better choice would be to fit adsorption energies, but unfortunately, these are usually not known experimentally. Another notable problem with the Hubbard correction is that the U value depends on the ion oxidation state, which changes from +2 to +4 during one reaction cycle (*vide supra*). Alternatively, one could use a U value derived from a linear response approach,[53] however, the empirical U fitted to redox enthalpies is a better choice because it relates both to reactant and product. Utilization of the on-site Coulomb correction is not that straightforward, in particular, for the surface calculations; however, omitting it would produce even larger errors, e.g., the magnetic

moment of Fe in the Fe doped CoO_2 is 1.98 μ_B at U = 0 eV. Alternatively, one could employ hybrid functionals; however, these are approximately two orders of magnitude more computationally expensive than DFT+U. Although hybrid functionals often provide higher accuracy, the question is to what extent they can improve the DFT+U results to warrant the excess computational cost. According to a recent study, the DFT+U yields slightly better Li intercalation potentials[54] compared to the popular Heyd-Scuseria-Ernzerhof (HSE) functional.[55] In another study, polaron hopping energies were found to be extremely sensitive to the choice of the mixing paremeter, which must be empirically fitted to match experiments, similarly as in the DFT+U approach.[56]

For dopants with unfilled *d* electrons we use a combination of calculated U values derived from fitting reaction enthalpies, and values in literature. For V, Cr, Cu, Mn and Fe we use 4.0,[57] 3.5,[58] 5.0, 2.8 and 5.0 eV, respectively, where the last three values are obtained by fitting to reaction enthalpies:

$$Cu + ½O_2 \rightarrow CuO \quad (3)$$

$$MnO + ½\ O_2 \rightarrow \beta\text{-}MnO_2 \quad (4)$$

$$FeO + H_2O \rightarrow \alpha\text{-}FeOOH + ½\ H_2 \quad (5)$$

It should be noted that in reaction (3) U is also applied on the 3d states of metallic copper. For other transition metals, we do not apply the U correction, either because they do not have d-electrons (e.g. Ti^{4+}, Nb^{5+}) or because their respective oxides have broad d bands (Ru, Ir, Pd and Rh), which substantially alleviates the effect of electron correlations.

As mentioned in the text, we use 4 different surface terminations, bulk terrace, bulk edge, NS terrace and nanosheet edge termination. The (0001) termination is made of periodically repeated 3 layer slab with a surface unit cell of 2x2 atoms. The (01-12) termination is represented by a 3 layer slab with the same 2x2 surface unit cell. The bottom layer is kept fixed to represent the bulk crystal, while remaining atoms and adsorbates are allowed to relax in order to assume minimum energy positions. In both cases, Brillouin zones are sampled by a 2x2x1 Monkhorst–Pack k-point grid,[59] which was sufficient to ensure convergence. For the NS terrace, we use a surface 2x2 atom cell and for the NS edge we use a larger 4x2 cell repeated in a surface direction perpendicular to the edge. Brillouin zones of nanosheet terraces and edges are sampled by the 2x2x1 and 1x2x1 Monkhorst–Pack k-point grids, respectively. A dipole correction is applied to electrostatically decouple

interactions of neighboring slabs in the surface normal direction for bulk surfaces and nanosheet terraces and in the direction perpendicular to the edge for nanosheet edges. The convergence is reached when the sum of absolute forces acting on the atoms becomes less than 0.05 eVÅ^{-1}. Activation barriers for association of oxygen atoms have been calculated with the nudged elastic band (NEB) method.[60,61]

The calculation of heats of formation of doped oxides is demonstrated on the examples of di-, tri-, tetra- and pentavalent ions (Eqs. 6-9).

$$\Delta E^{form} = E(Co_{0.75}Mg_{0.25}O_2H_2) - \tfrac{3}{4}E(CoO_2) - \tfrac{1}{4}E(MgO) - \tfrac{1}{4}E(H_2O) + \tfrac{1}{4}T\Delta S(H_2O) \quad (6)$$

$$\Delta E^{form} = E(Co_{0.75}Fe_{0.25}O_2H) - \tfrac{1}{2}(3/4E(CoO_2) - 1/8E(Fe_2O_3) - 1/8E(H_2O) + 1/8T\Delta S(H_2O)) \quad (7)$$

$$\Delta E^{form} = (Co_{0.75}Ni_{0.25}O_2) - \tfrac{3}{4}E(CoO_2) - \tfrac{1}{4}E(NiO_2) \quad (8)$$

$$\Delta E^{form} = E(Co_{0.75}Nb_{0.25}O_2) - 3/4E(CoO_2) - 1/8E(Nb_2O_5) + 1/16E(O_2), \quad (9)$$

, where ΔE^{form} is the formation energy. Hydrogen atom(s) are added to oxygens to correct to the desired valence, e.g. for trivalent elements (Al, Ga, In, Ag) a hydrogen atom is added on an oxygen ion to which the dopant is coordinated, and for divalent dopants (Mg, Cu, Zn, Cd) two hydrogens are added on two vicinal oxygen ions (see Note 1 in the ESI). We assume the same ZPE for elements in solid compounds. For entropy of water and oxygen we use 0.67 and 0.64 eV, respectively, according to Ref. [62]. It is a well-known fact that DFT notoriously overestimates the oxygen binding energy.[63] For this reason, we correct the energy of oxygen by 0.4 eV, which is the difference between the calculated and experimental reaction free energy of water formation: $\tfrac{1}{2}O_2 + H_2 = H_2O$.

The approach for calculating heats of formation of anion-intercalated electrodes is formulated in Note 1 in the Electronic Supporting Information (ESI).

3. Results and discussion

3.1. Pristine catalysts

Bulk materials are modelled by 3 ox-hy layers and nanosheets (NS) by a single oxide layer. We choose the two most stable, (0001) and (01-12), facets.[22,64] The (0001) termination exposes terrace sites, whereas the (01-12) termination (a tilted (0001) surface) represents in fact a bulk edge termination. There are two general rules to follow when creating the ox-hy slab. The first, each

metal ion should be coordinated to 3OH and 3O ligands. For Co ox-hy, this coordination is 0.26 eV more stable than the antisymmetric coordination, in which neighboring Co ions are coordinated to 2OH/4O and 4OH/2O ligands, respectively (see Note 2 in the ESI). The second, the orientation of polar hydroxyl species has a large influence on the electronic structure of the 2D and 3D terraces (cf. Figure 1). If OHs are preferentially aligned in one direction, the resulting dipole is huge, triggering a partial charge transfer from the lower to the upper oxide sheet. Effectively, this creates a p- and a n-type semiconductor from the bottom and top layer of the slab, respectively, which is evidenced in the electronic DOS by pinning of the Fermi level to either the valence or conduction band edge. Charge separation generates a dipole in the opposite direction that counteracts the intrinsic dipole. It is noteworthy that this effect takes place even though a dipole correction is included in the simulations. Charge separation will influence the binding energies of OER intermediates, such that they will be overestimated on one side and underestimated on the other side of the slab. This spurious effect can be avoided if the dipoles are oriented in such a way that their net sum approaches zero (see Figure 1b). With no or a very small net dipole, there is no charge transfer, indicated by the position of the Fermi level (vertical solid line at *E-Ef = 0*) right at the middle of the band gap.

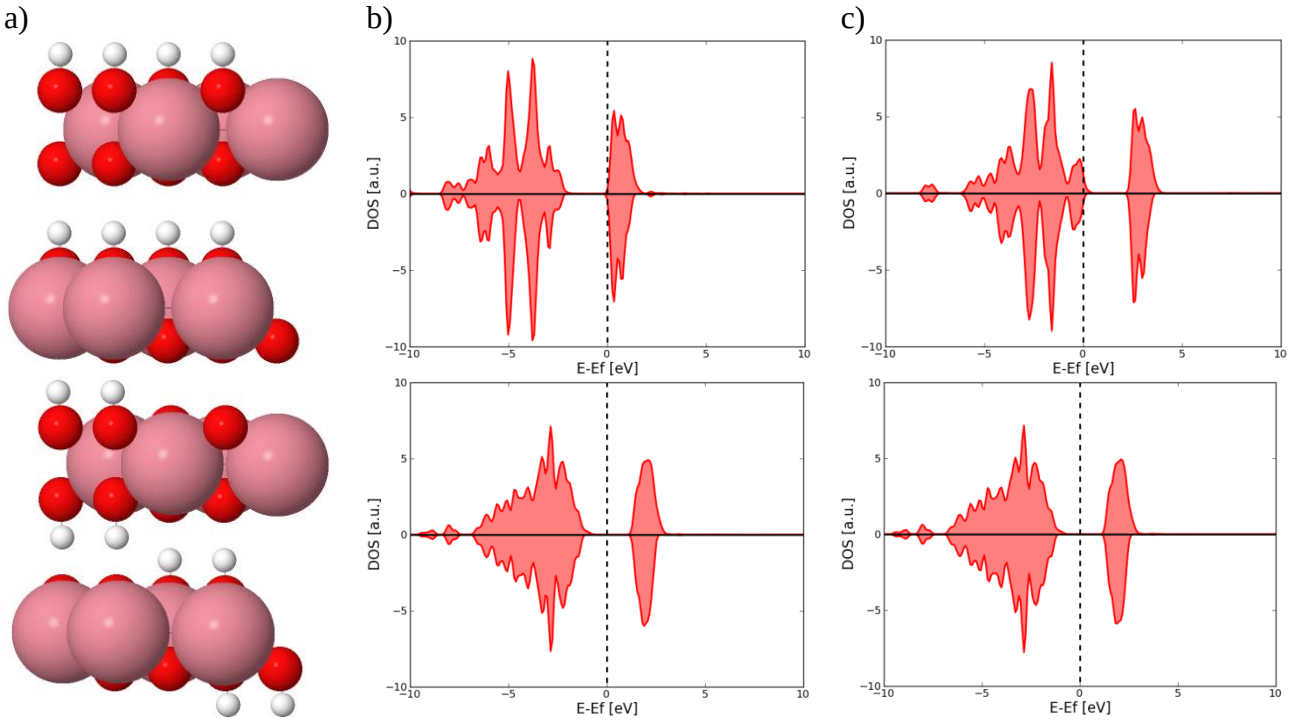

Figure 1 a) Different arrangement of OH dipoles in a Co oxyhydroxide bilayer and the resulting density of states for the b) top and c) bottom layer. Position of the Fermi level (E - Ef = 0) at either band edge indicates a partial charge transfer.

The oxidation state of Co and Ni ions changes from +3 to +4 at slightly higher potentials than the equilibrium potential for water oxidation.[65] Experimentally, activities of Co ox-hy and Co_3O_4 have been found to correlate well with the population of the Co^{4+} and Ni^{4+} species.[17,66–71] Thus, increasing the number of Co^{4+}/Ni^{4+} sites at a constant potential would enhance the oxygen evolution currents. As a first step in our analysis, it is necessary to calculate the surface oxidation state at relevant OER conditions for each termination. In a commonly employed theoretical mean-field approach, the reaction overpotential is approximated by the potential at which the largest electrochemical step becomes reversible in free energy.[62] This is a purely thermochemical measure, and cannot be directly associated with the experimental onset potential unless charge transfer, surface kinetics and time scales of processes at the interface are very fast. Furthermore, as it is hard to define exactly the onset potential in experiments, the overpotential is commonly stated at a specific benchmarked current density, i.e. oxide catalysts,[6] or a half-way potential, e.g. metal catalysts.[72] The reaction overpotential is greatly dependent on the current density at which it is measured. Experimentally, OER catalysts are benchmarked at a current density of 10 mA/cm^2.[6] It should be however noted that such a low current density is not relevant for all industrial applications. It is appropriate for metal-air batteries and photoelectrochemical devices, but not for water electrolyzer cells, which operate at one or two orders of magnitude higher current densities.

3.1.1. Surface Termination

The oxidation state of the surface ions changes as a function of potential. In order to obtain the pertinent surface, it is necessary to assume *a priori* the potential at which the reaction operates. In fact, to be fully consistent, the surface termination should not be assumed *a priori*, but calculated iteratively as long as the reaction overpotential does not fall in the same stability range as the surface for which it has been calculated. Here, we assume the overpotential of 0.5 V versus RHE, which can be approximately regarded as an average overpotential between the low and high current density limits. Another reason we choose the 0.5 V overpotential and not higher is to avoid parasitic hydrogen peroxide evolution that sets in at 1.78 V vs. RHE.[65]

We determine the stable surface oxidation for Co and Ni ions in the ox-hy NS and then tune the surface oxidation state in the other terminations accordingly. The variation of the surface oxidation state on potential is computed through Co and Ni ox-hy dehydrogenation isotherms (see Note 3 in the ESI). In practice, this is done by successively removing H atoms from Co ox-hy NS and finding a thermodynamic free energy barrier for this process. We find that Co and Ni ox-hy nanosheets become fully oxidized to NiO_2 and CoO_2 already at 1.4 V. We adjust the valence of surface ions in the other terminations to nominal 4 by adding hydroxyl groups (electron acceptors) and/or removing hydrogen atoms (electron donors).

In the case of the (0001) facet, the surface is composed of the 50% - 50% mixture of Co^{3+}/Ni^{3+} and Co^{4+}/Ni^{4+}. The average Ni valence measured experimentally in Ni ox-hy is 3.67,[73] which agrees nicely with the 3.5 value calculated herein. Co^{3+}/Ni^{3+} are present on the surface because strong hydrogen bonds between the sheets prevent its oxidation to +4. These hydrogen bonds can be removed by ion intercalation.

3.1.2. Reaction mechanism

After establishing the surface oxidation state, we calculate the overpotential invoking the computational hydrogen electrode (CHE)[62]. We consider three different reaction mechanisms, one at a single site and two involving two adjacent surface sites.

In the first mechanism, a hydroxyl group first attacks the oxide surface (step (1)). We find this step to be a PDS for bulk and NS terraces. The surface hydroxyl subsequently deprotonates to O^* (step 2), creating an $^*O_2$ intermediate with the lattice oxygen that desorbs from the surface. Another hydroxyl group then discharges to the vacancy left by O_2 (step 4). After a second deprotonation step (step 5), the initial surface is fully restored.

$$^* + OH^- \rightarrow {}^*OH + e^- \qquad \text{(step 1)}$$

$$^*OH + OH^- \rightarrow {}^*O + H_2O + e^- \qquad \text{(step 2)}$$

$$^*O \rightarrow {}^*O_{vac} + O_2(g) \qquad \text{(step 3)}$$

$$^*O_{vac} + OH^- \rightarrow {}^*H + e^- \qquad \text{(step 4)}$$

$$^*H + OH^- \rightarrow {}^* + H_2O + e^- \qquad \text{(step 5)}$$

, where * is the available surface oxygen site, and $^*O_{vac}$ is the oxygen vacancy created after O_2 desorption. Notice that in between the four electrochemical steps, there is also a purely chemical step for O_2 desorption (step 3). This step is usually disregarded, which is justified by the fact that O_2 does not adsorb or adsorbs weakly to the surface. In principle, O_2 could adsorb strongly to the surface making the chemical desorption step the rate-limiting step.

In the second mechanism, the first step is the recombination of two neighboring lattice oxygens to form O_2 (step 6).

$$2^* \rightarrow {}^*O + {}^*O_{vac} \rightarrow O_2(g) + 2^*O_{vac} \qquad \text{(step 6)}$$

$$2^*O_{vac} + 2OH^- \rightarrow 2H^* + 2e^- \qquad \text{(step 7)}$$

$$2H^* + 2OH^- \rightarrow 2^* + 2H_2O + 2e^- \qquad \text{(step 8)}$$

The following steps in the reaction cycle are two hydroxylation steps (step 7) of the O vacancies and their further oxidation (step 8) to recreate the initial surface. Step (6) circumvents steps (1) and (2) in the first reaction mechanism. Step 6 is viable only if it is energetically more facile than steps (1) and (2). We have computed activation barriers for step (6) using NEB on three representative terminations, i.e. a nanosheet terrace, nanosheet edge and bulk edge, where oxygen is 3-, 2- and 1-fold coordinated to Co ions. For the 3- and 2- fold oxygen activation energies are 1.96 and 1.11 eV, respectively rendering the second reaction path unfeasible. On the surface of bulk edge the barrier is much lower (0.23 eV) because O moieties are not stable (*vide supra*) and therefore can easily react off to form O_2(g). This step should be considered only if step (1) or (2) are the PDS.

The third reaction mechanism is a disproportionation mechanism, wherein reaction step (2) is circumvented by disproportionation of adjacent hydroxyl intermediates (step 11) to make water, oxygen and a surface oxygen vacancy.

$$^* + {}^*OH + OH^- \rightarrow 2^*OH + e^- \qquad \text{(step 9)}$$

$$2^*OH \rightarrow O^* + {}^*OH_2 \rightarrow {}^*O_{vac} + O_2(g) + {}^* + H_2O \qquad \text{(step 10)}$$

Step (10) consists of two consecutive steps, proton transfer between two hydroxyl intermediates and subsequent evolution of O_2 and H_2O. We do not study proton transfer steps because they are usually considered to be fast.[74] Step (10) is preceded by two formation steps of hydroxyl intermediates (step 1 and 9) and followed by filling of the oxygen vacancy (step 4 and 5),

which completes the thermodynamic cycle. This reaction pathway will be considered only if step (2) is the PDS. For the zero point energy and entropy corrections for the OH, O and OOH intermediates, we use values of 0.35, 0.05 and 0.4 eV, respectively.[62] Furthermore, we assume that OH^- comes from OH^- in the solution. Alternatively, a water molecule can also bind to a vacant site and discharge a proton. We expect water discharge to have a higher barrier than a simple OH^- adsorption. The water dissociation step should be however taken into consideration in acidic environments, where there are very few hydroxyl ions present.

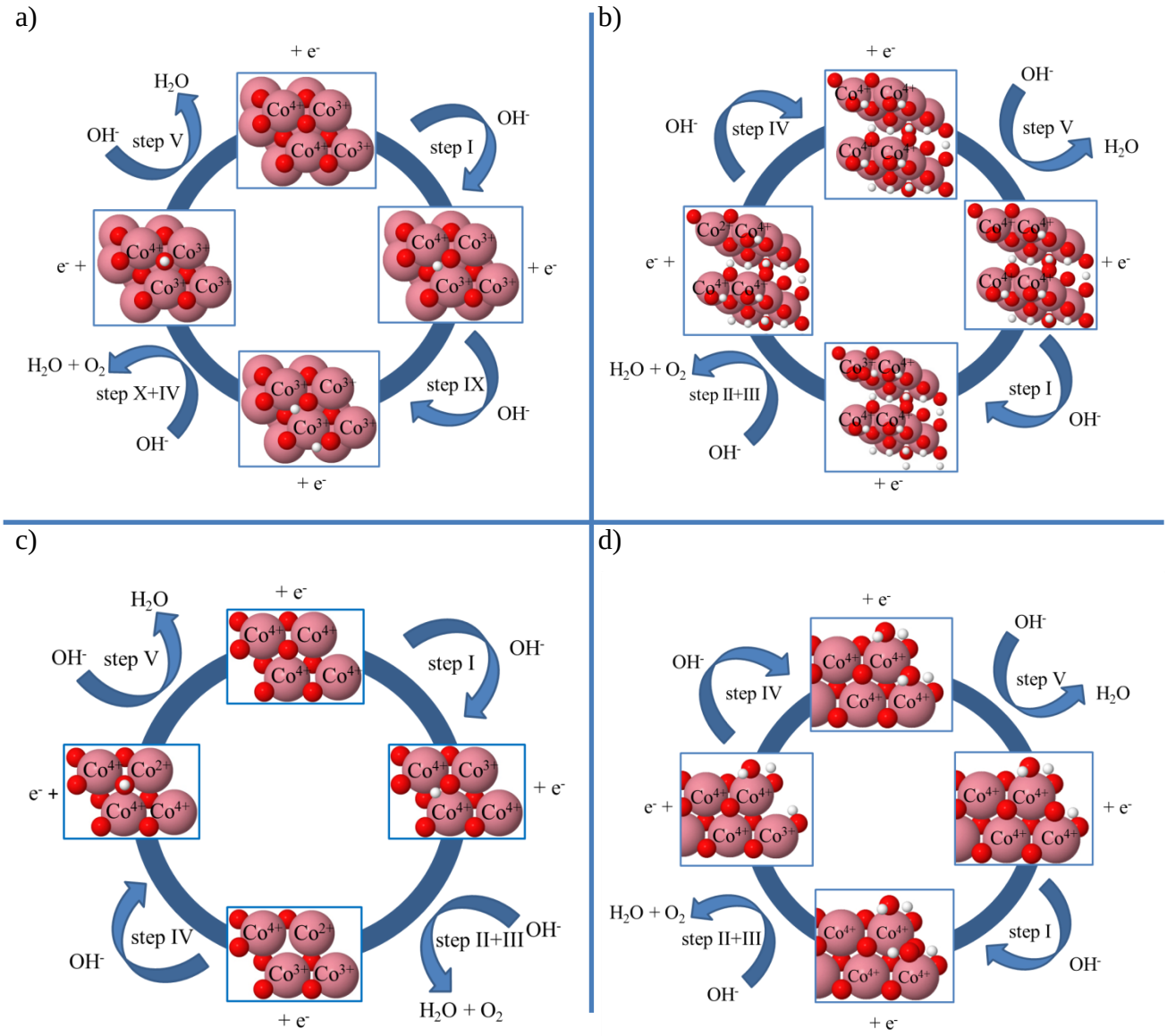

Figure 2 Illustrations of the oxygen evolution mechanism on a) bulk terrace, b) bulk edge, c) nanosheet terrace and d) nanosheet edge of Co oxyhydroxide. Illustrations are not periodically repeated.

The minimum energy paths on the examples of the different Co ox-hy terminations are presented in Figure 2. Magnetic moments of terminal Co ions are denoted for each step of the cycle. Every cycle starts from stable surface termination at the top of the reaction scheme. Notice that the starting structure is surface termination dependent; for terrace sites it is the O terminated surface and for edge sites it is the OH terminated surface.

3.1.3. Catalytic Activity

Activities of the different terminations are compared in Figure 3 according to reaction overpotentials. From a theoretical perspective, reaction overpotentials are identified with the minimum potential required to make all electrochemical steps exergonic in free energy minus the reversible potential for reaction.[62] The difference between the four surface terminations is in the coordination of the active site. On bulk and NS terraces, the active site is coordinated to three metal ions; on nanosheet edges to 2 metal ions and at bulk edges only to a single metal center. As we shall see later, the different coordination has important consequences on the activity.

For all the studied terminations, the reaction proceeds through the 1st reaction pathway except for the bulk Co ox-hy terrace, where the 3rd mechanism is the preferred path. Several conclusions can be drawn from Figure 3. First, the OER overpotentials increase going from 3D to 2D on terraces, whereas the opposite effect is observed at the edges. Secondly, Ni ox-hys are in general more active catalysts than their Co counterparts; with the only exception being bulk edge. The higher activity of the Ni ox-hy is rationalized by the fact that Ni favors less than Co to be +4, rendering the fully oxidized surface less stable and the PDS (step 1) lower in energy than on Co ox-hys. The situation is different at the bulk edge termination, where the PDS is OH oxidation to O (step 2). As neither Co nor Ni favor the 5 valence, the oxygen intermediate in both cases is more O^- than O^{2-} like. The same argument can be used to explain the low activation barrier for making O_2. The finding that Ni is more active than Co ox-hys is in agreement with most experimental and theoretical studies in literature.[22,52,73,75] It should be however noted that in several recent studies, the high activity of Ni ox-hys was ascribed to the presence of Fe contaminants, and the Fe-free Ni ox-hys was in fact found to be less active than its Co counterpart.[6,11]

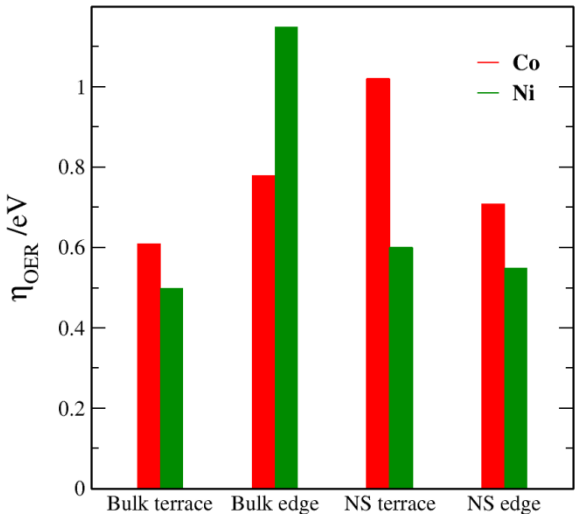

Figure 3 Oxygen evolution activity measured by reaction overpotentials (η) for Ni (green) and Co (red) oxyhydroxide terminations. Bulk terrace and edge denote respectively the (0001) and (01-12) surface termination. NS stands for nanosheet.

3.1.4. Electronic conductivity

Electronic structure is a fingerprint of electron conductivity. Figure 4 shows DOS plots for the different ox-hy terminations. To a first approximation, the electronic conductance is measured by the occupancy of the electronic states at the Fermi level. As expected, we find the band-gap to increase with U (see Note 4 in the ESI). For the selected U values, the theoretical band gaps are close to experimental values of 2.0 eV for CoOOH[76] and 1.8 eV for NiOOH.[77] According to crystal field theory, Co^{3+} and Ni^{4+} are paramagnetic ions in the octahedral geometry, with completely filled t_{2g}, empty e_g orbitals and the band gap in-between. The semiconducting behavior is seen for Co^{3+} in CoOOH (cf. Figure 4a) and for Ni^{4+} in the NS (cf. Figure 4d). There are both Co^{3+}/Ni^{3+} and Co^{4+}/Ni^{4+} surface metal ions at the (0001) termination. In a classical band description, one would expect Co^{4+} to have a metallic character owing to partial filling of the t_{2g} orbitals. However, a strong electron correlation in the 3*d* orbitals makes Co^{4+} a semiconducting ion (cf. Figure 4c and d). In contrast, the bulk Ni terrace is half-metallic because Ni^{3+} has one unpaired e_g electron that frontally overlaps with the oxygen 2p orbitals, thus giving rise to broad hybridized states at the Fermi level (cf. Figure 4b). The Ni (01-12) termination is also electronically conductive due to a partial charge transfer between surface O and Ni^{4+} ions. Typically, whenever Ni^{3+} is present at the surface, the charge is more delocalized, evidenced by the absence of Jahn-Teller distortions and charge delocalization over neighboring Ni ions. In summary, we find Ni^{3+} to be more electronically conductive than the other Ni and Co valences.

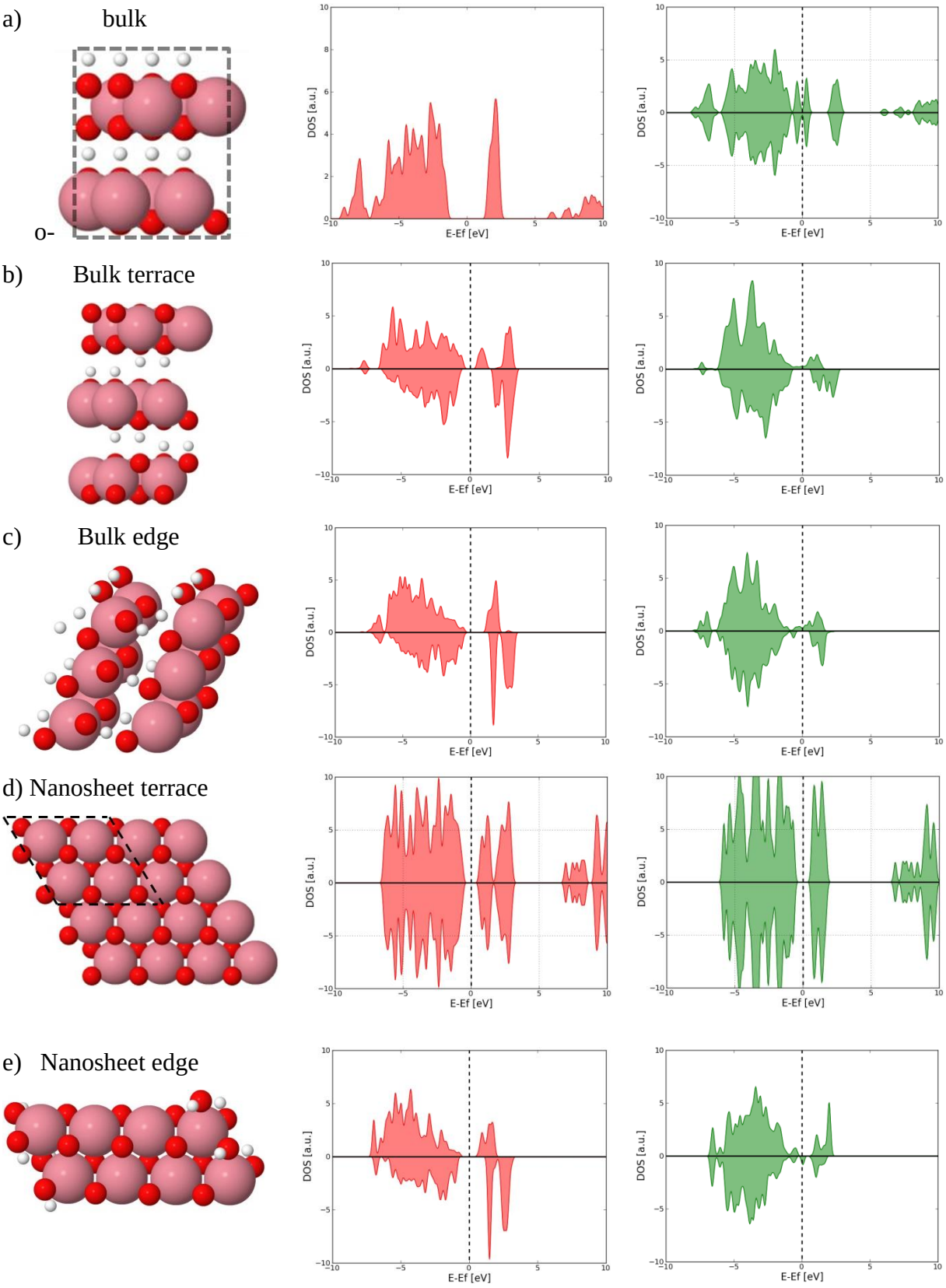

Figure 4 Illustrations of the different terminations and density of state plots for the a) bulk crystal and b) bulk terrace, c) bulk edge, d) nanosheet terrace and e) nanosheet edge surfaces of Co (red) and Ni (green) oxyhydroxides. For b, c and e, density of states are projected on the topmost surface

layer or edge atoms to distinguish the surface/edge from bulk conduction. Black dashed lines are bulk and nanosheet unit cells.

3.2. Doped catalysts

To investigate the effect of doping, we have initially chosen a pool of 25 different doping elements (V, Cr, Mn, Fe, Co/Ni, Cu, Ru, Rh, Pd, Ir, Pt, Ag, Al, Ga, In, Sn, Pb, Bi, Mg, Sc, Y, Ti, Nb, Zn and Cd), which all form stable oxides in the pH range from neutral to alkaline. First, we conduct the analysis on the simplest termination, i.e. the NS terrace. We narrow the initial set of catalysts using structural stability, OER activities and electronic conductivities as selection criteria. Afterwards, we extend the analysis to include bulk terminations and NS edges, but only for dopants stable at NS terraces.

3.2.1. Stability

On the fully oxidized NS surface, all metal ions are in the +4 oxidation state. As chemical reference, we use oxide in which the dopant ion is in the same oxidation state as in the ox-hy NS (see Note 5 in the ESI). Stabilities are evaluated through heats of formation of the doped oxides.

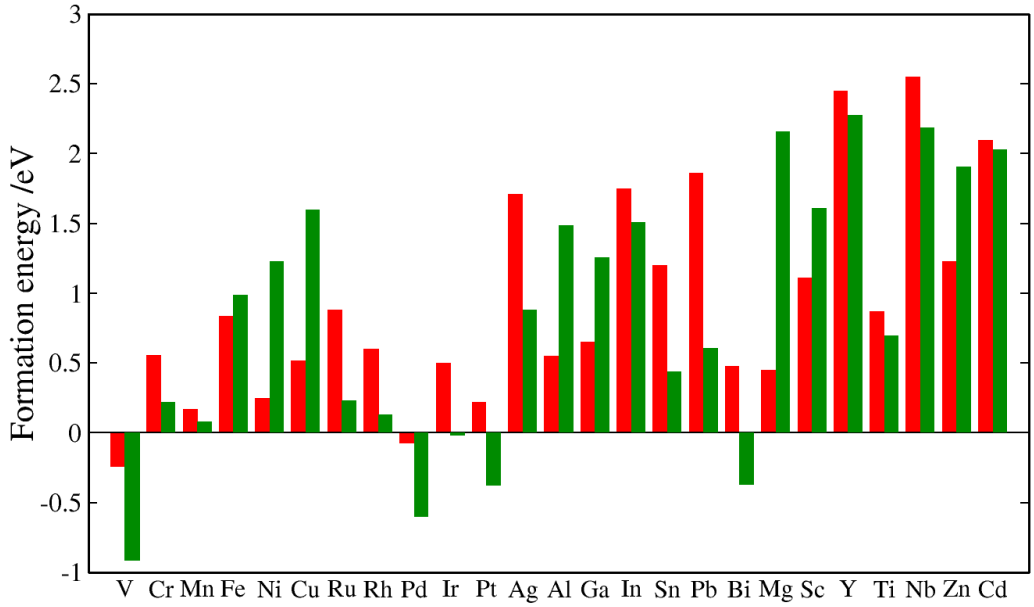

Figure 5 Calculated formation energies of doped Co (red) and Ni (green) nanosheets against the most stable individual (host + dopant) oxide phases in the potential stability range of $Co(OH)_2$/$Ni(OH)_2$.

Heats of formation of the doped ox-hy NS are presented in Figure 5. The concentration of dopants is restricted to ¼ ML. In this limit, we do not expect the Ni and Co oxide lattice to change appreciably with doping. As seen in Figure 5, it is generally more facile to dope Ni than Co ox-hys. Certain first row transition and noble metals are characterized by relatively low heats of formation. Positive values indicate that most doped oxides are in fact not stable. It is particularly striking that Fe, which is otherwise known to self-incorporate into Ni and Co ox-hys,[38,41,46] is not among the stable dopants. In order to reconcile this apparent contradiction, we have systematically investigated the incorporation of dopant ions in LDH - the ox-hy precursors. LDH is a disordered, non-crystalline phase of metal di-hydroxide with positively charged sheets and charge balancing ions intercalated between the sheets. There also exists a non-charged, ordered phase composed of stacked brucite-like layers. Apart from the difference in the oxidation state of the metal ions, the two phases differ in the intersheet registry. For a more detailed discussion about the structural differences between ordered and disordered hydroxide and ox-hy phases we refer to a recent review article.[25] For divalent dopants, we calculate heats of formation within the brucite layers and for dopants with valence higher than 2, we use the LDH structure, in which the excess charge is compensated by intercalation of Cl^- ions inside the oxide sheets (see Note 1 in the ESI). Thus computed heats of formation are presented in Figure 6. It is noteworthy that reference oxides are not necessarily the same for ox-hys and LDHs (cf. Note 5 in the ESI) because of different potential stability ranges of the two materials. We find formation energies to increase with valence for the same dopant, e.g. the free energy for incorporating Ni^{+3} is 0.37 eV higher than that for Ni^{+2}.

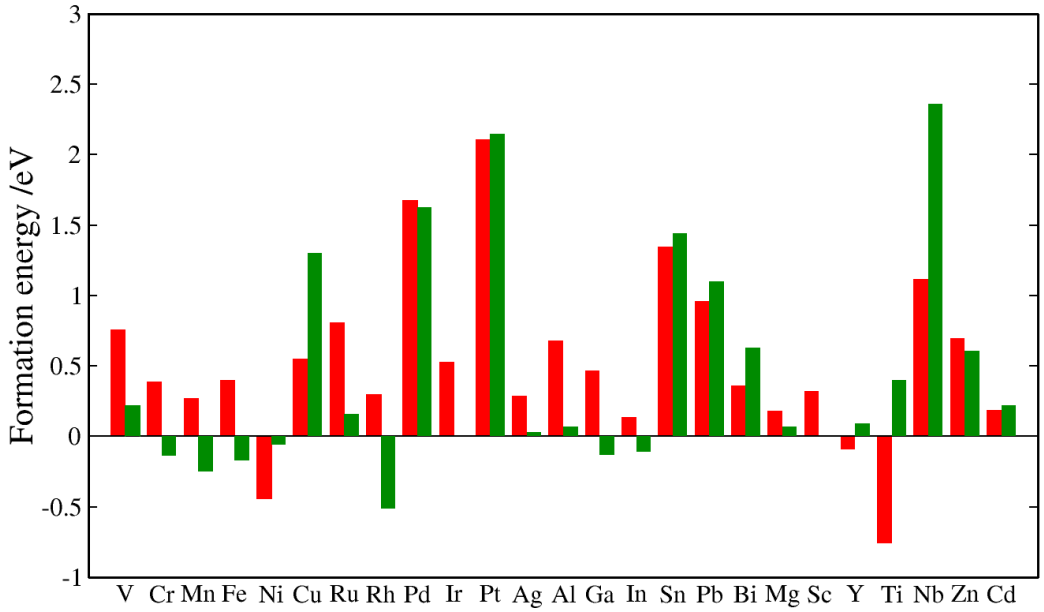

Figure 6 Calculated formation energies of Co (red) and Ni (green) hydroxides against the most stable individual (host + dopant) oxide phases in the potential stability range of CoO_2/NiO_2.

By comparing Figure 5 and Figure 6, it becomes immediately obvious that formation energies of the doped hydroxides are greater than those for the doped ox-hy NS. This result suggests that doped hydroxides stable in the low potential limit might become thermodynamically unstable at potentials relevant for OER, as it is the case for Fe doped $Ni(OH)_2$. However, such catalysts might be kinetically stable against phase segregation because of high energies for making vacancies in the NS. It should be noted that estimates in Figure 5 and Figure 6 are based on the calculated heats of formation; as such they do not take into account the kinetic stability *per se*.

3.2.2. Catalytic activity

Following the approach for the pure oxides, we first determine the most stable surface termination at OER potentials by computing dehydrogenation isotherms for the doped Co ox-hy nanosheets (cf. Note 3 in the ESI). To reduce the computational cost, we assume the same oxidation state of the surface for the doped Ni NS. The conclusion is that most of the doped oxides are fully oxidized at the benchmarked potential of ca. 1.7 V, with the exception of several dopants that favor +2 or +3 oxidation state (Al, Ga, Mg, Sc and Y). As reaction overpotentials on all these catalysts are much greater than 1.7 V, their surfaces will be fully oxidized too at operating potentials.

Table 1 Change in valence during oxygen evolution cycles, calculated reaction overpotentials (η) and estimated electronic conductance for the doped oxyhydroxide nanosheets.

		Doped Co ox-hy		**Doped Ni ox-hy**	
	valence	η /V	conductance	η /V	conductance
V	4-5	0.93	No	0.41	Yes
Cr	3-4	0.56	Yes	0.56	Yes
Mn	4	1.52	No	1.19	No
Fe	3-4	0.70	Yes	0.43	Yes
Ni/Co	4	0.93	No	0.86	No
Cu	2	0.45	Yes	0.57	Yes
Ru	4	0.98	Yes	0.37	Yes
Rh	4	1.12	Yes	0.57	Yes
Pd	4	1.13	No	0.69	No
Ir	4	1.33	Yes	0.55	Yes
Pt	4	1.23	No	0.78	No
Ag	3	0.75	Yes	0.52	Yes
Al	3	0.67	No	0.61	No
Ga	3	0.68	No	0.64	No
In	3	0.49	Yes	0.52	Yes
Sn	4	1.12	No	0.75	No
Pb	4	0.47	No	0.69	No
Bi	5	0.53	Yes	0.75	Yes
Mg	2	0.92	No	0.73	No
Sc	3	0.63	No	0.74	No
Y	3	0.62	No	0.64	No
Ti	4	0.85	No	0.34	No
Nb	5	0.54	No	0.63	Yes
Zn	2	0.46	Yes	0.50	Yes
Cd	3	0.39	Yes	0.39	Yes

After establishing stable surface terminations, we calculate reaction overpotentials and qualitatively assess electron conductivities through the analysis of the electronic DOS. We find that for all the doped NS, the reaction proceeds through the 1st reaction mechanism, with either step (1) or step (5) being the PDS. We have previously excluded the 2nd reaction mechanism due to very high activation barrier for oxygen association and the 3rd pathway will be limited by the same step (1) or (5) it shares with the 1st reaction mechanism. Free energy values for all the different electrochemical steps (steps 1, 2+3, 4, and 5) and DOS plots for all the NS surfaces are compiled in Notes 6 and 7 in the ESI.

3.2.3. Electronic conductivity

According to Table 1, the electronic conductance is strongly dependent on the metal dopant, and much less on the host metal oxide. The only exceptions are the V and Nb doped NiO_2 that are conducive to electron transport in contrast to their Co counterparts. Nb prefers the +5 oxidation state, thus forcing one Co^{4+}/Ni^{4+} ion to Co^{3+}/Ni^{3+} in order to maintain charge neutrality inside the material. The difference in electron conductivity of Ni^{3+} and Co^{3+} explains why Nb doped NiO_2 is a better electron conducting material compared to Nb doped CoO_2. For the V dopant, a different effect is at play. The strong hybridization between the Ni 3d, V 3d and O 2p states results in delocalized electronic states at the Fermi level, giving rise to good electronic conductivity (see Note 7 in ESI).

In Figure 7, we bring out four different cases, each with a different origin of electronic conduction. We start out with the Fe doped Co ox-hy NS. Fe in the fully oxide nanosheet has a magnetic moment of 3.91 μ_B. This magnetic moment is ascribed to Fe^{4+}. The magnetic moment of Fe^{3+} in a partially reduced sheet is 4.59 μ_B, which corresponds approximately to Fe^{3+}. Fe is otherwise not known to be stable as Fe^{4+} in oxides or polyionic oxygen compounds.[78] Fe^{4+} has one electron in the e_g-dz^2 orbital that overlaps frontally with the oxygen $2p_z$ orbital, forming a σ bonding orbital. A broad σ band straddles the Fermi level and gives rise to electronic conductivity. In support of the charge delocalization and the metallic nature of the NS is the absence of Jahn-Teller distortions, which are known to occur readily for ions with nominal e_g values of 1. In some experimental studies, Fe^{4+} was hypothesized to be the active site of the NiFe catalyst, [38,69] whereas other studies claimed that it is not Fe^{4+} but actually Fe^{3+}.[71] We have compared the overpotentials for Fe^{3+} and Fe^{4+} in the Co ox-hy NS and found a very small difference of 0.03 V.

To exemplify the second case, we take the Cu dopant. From a magnetic moment analysis, the Cu ion is +2 and Co +4. In principle, Cu should be +4 too in order to satisfy charge balance in the material, however, this is not the case because vicinal oxygen atoms donate a portion of negative charge δ to Cu ions. Widtrawal of charge from oxygen is supported by a change in the oxygen magnetic moment from 0 to approximately 0.15 μ_B. The hole that is left is almost unifomly distributed over oxygen ions in the cell. Cu doped CoO_2 is electronically conductive and the Fermi level is positioned right at the valence band edge. This catalyst is not a lone example of this class; in fact all doped systems that are fully oxidized at 1.7 V and whose dopants favor valence lower than 4, have the same electronic stucture. Most of these systems will likely decay to an oxygen deficient material, as it happens for perovskite oxides with holes on oxygen ions.[79]

For the Rh doped CoO_2 NS, the good electronic conduction is mostly coming from the Rh 3d states. Rh, Ir and Ru rutile dioxides are different from other transition metal oxides because they are characterized by good electronic conduction. The existence of broad d bands breaks the degeneracy of the d states and gives rise to high DOS at the Fermi level. Apparently, this group of dopants displays the same atomic scale bevahior when incorporated into Co or Ni ox-hys.

The fourth representative example is the Bi doped CoO_2 NS. Bi is +5 and has a higher oxidation state than +4. Since the unoccupied Co 3d states are closer in energy to the Fermi level than the O 2p states (compare DOS for pristine and Bi doped CoO_2 in Note 7 in the ESI), the positive charge at the Bi ions is compensated by a negative charge delocalized over neighboring Co ions, thereby effectively changing the oxidation state of cobalt from Co^{4+} to $Co^{3+\delta/3}$. Bi-doped NS will most likely not display the long term stability and are expected to undergo transformation to a structure with a higher Bi-O coordination such as e.g. V_2O_5 or (even more probable) decay to a mixed Bi_2O_5 and Co oxide phase. As can be concluded from the examples above, the dopant ion's valence plays a critical role for assessing the catalyst stability.

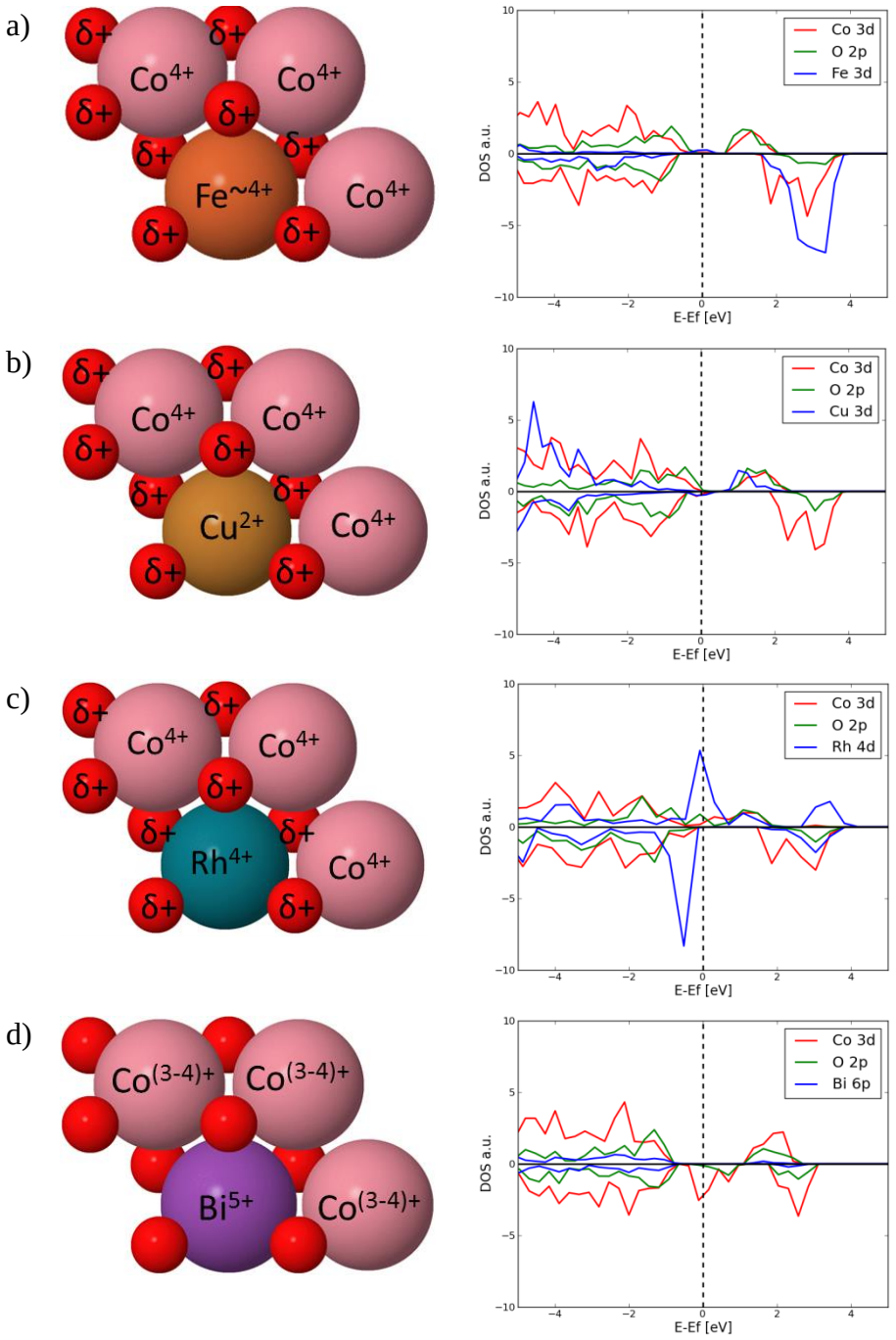

Figure 7 Projected density of states onto the Co 3d, O 2p and the highest occupied dopant states for the four representative cases: the a) Fe, b) Cu, c) Rh and d) Bi doped CoO_2 nanosheet.

The most active Co ox-hy catalysts are those with di- and trivalent dopants, whereas tetravalent elements show very poor activity for oxygen evolution (see Table 1). In the case of the Ni ox-hy NS, certain tetravalent noble metals (Ru, Rh and Ir) decrease significantly the reaction overpotential with respect to the non-doped catalyst. The PDS is dependent on the oxidation state of the dopant ion. For dopants that favor the +4 valence (Mn, Ru, Pt, Pd etc.), PDS is the addition of a hydroxyl

ion to form an oxyhydroxyl intermediate (step 1); for those that favor +2 or +3 oxidation state (Cu, Cd, Mg, Al, Ga, In etc.), the bottleneck for the reaction is the last step (step 5), i.e. the oxidation of a surface OH to form a fully oxidized surface.

Another important conclusion is that electronic conductivity does not only depend on the dopant atom, but also on the valence. For e.g. transition metal elements, the valence changes as a function of potential. The potential dependence of the conductivity is exemplified by the Fe doped CoO_2 NS. At potentials below 1.5 V, the surface is partially reduced meaning that Fe is Fe^{3+}. As Fe^{+3} is not a conductive species the Fe doped NS is an insulator. At potentials above 1.5 V, the surface becomes fully oxidized and the presence of Fe^{4+} with partly filled e_g orbital gives rise to good electronic conductivity (cf. Figure 8). The same abrupt change in the conductivity is seen for di- and trivalent dopants; albeit due to presence of oxygen holes and not the metal 3*d* states.

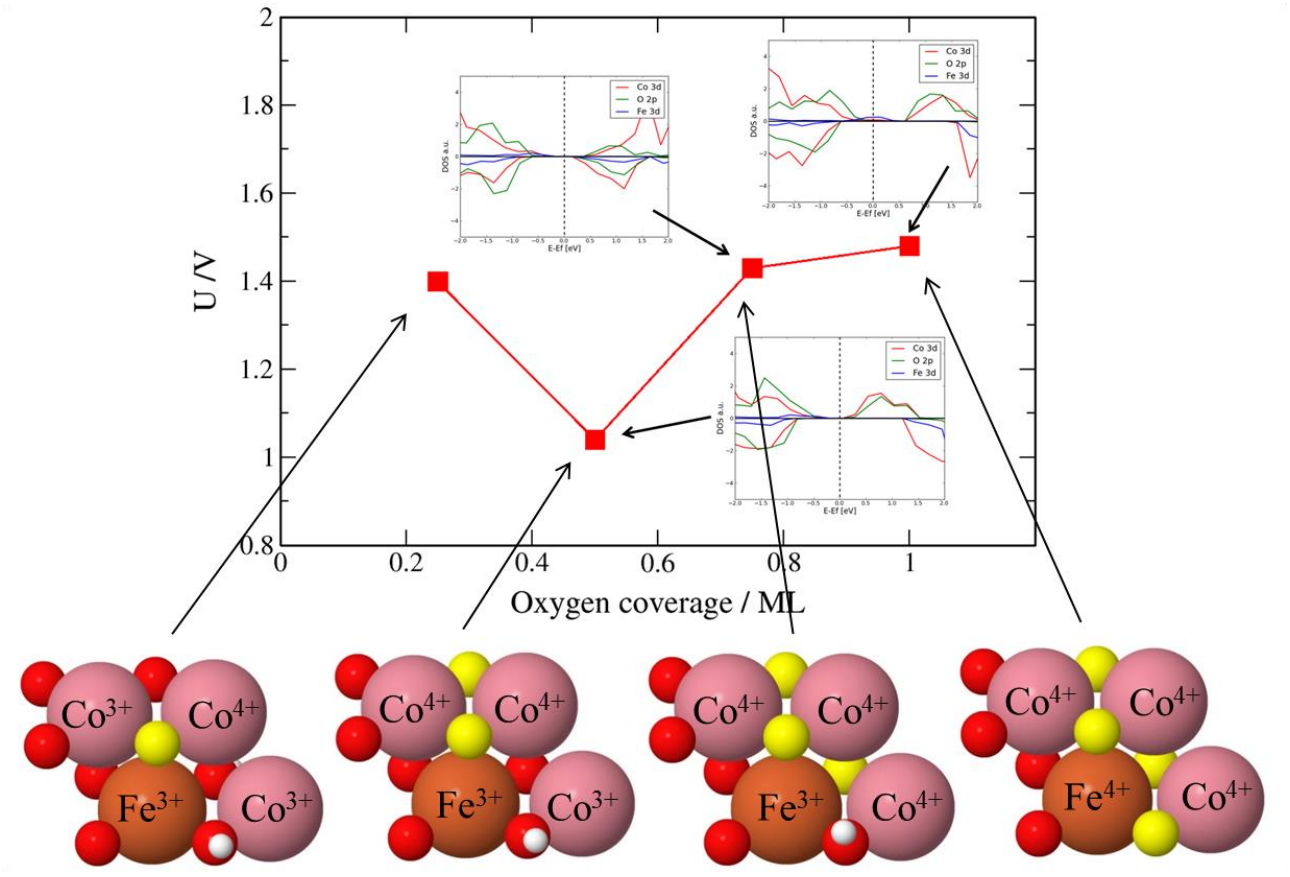

Figure 8 Electronic conductivity as a function of potential on a Fe doped Co oxyhydroxide nanosheet. The red line is the oxygen adsorption isotherm drawn through discrete points at different oxygen coverages. The insets show the corresponding density of states and the illustrations show the evolution of oxidation states at different coverages measured by the number of oxidized OH moieties (in yellow) per metal atoms in the unitcell.

We select the best dopants on the basis of formation energies, reaction overpotentials and electronic conductivities reported in Figure 5 and 6, and Table 1. Doped NS with a relatively low heat of formation, low overpotential for oxygen evolution that are conducive to electron transport are Fe, Cr doped Co ox-hy and V, Cr, Fe, Ru, Rh and Ir doped Ni ox-hy NS. Thus, from the initial pool of 50, we have narrowed the selection to approximately 10 candidates that seem to fulfill the stability, activity and conductivity criteria.

3.3. Doped bulk catalysts

3.3.1. Stability

Thus far we have only discussed the effect of doping on the NS terraces. In a bulk system, it is important to consider surface segregation, which shows the preference for dopant atoms to sit in the subsurface layers or the surface layer. Dopants that prefer the bulk over the surface sites can affect electronic transport only, whereby those that segregate to the surface can prompt activity by reducing the reaction overpotential. Both properties are important aspects of a good electrocatalyst. Ideally, a doping element should have a flat segregation profile and contribute both by increasing activity at the surface and by promoting electronic conduction in the bulk. Alternatively, one could consider a multicomponent system, where the role of one dopant is to increase the bulk conductivity and the other to accelerate the reaction rate at the surface. An important difference between the subsurface and surface ions is that the former are always +3, whereas the latter can be either +3 or +4, depending on the surface termination. Here, we consider both surface sites and use the more stable values to make segregation profiles shown in Figure 9 (see Note 8 in the ESI for the direction of segregation). A negative energy difference indicates that dopants are more stable at the surface/edge than bulk/terrace. The results suggest that noble metals prefer to segregate to the surface, where they can become +4. Moreover, they also favor to be at the edges of the NS, probably because they have lower surface energies compared to CoO_2 or NiO_2. Edge segregation occur also for dopants that prefer valence higher than 4 (e.g. V), because at edges they can further oxidize by formation of O from terminal OH. Cr, on the other hand, favors +3 sites, whether on the surface or in bulk. Fe is unique in a sense that it can be both +3 and +4, which explain a relatively flat segregation profile. Unfortunately, neither Fe^{3+} nor Cr^{3+} promote electronic conductivity in the bulk.

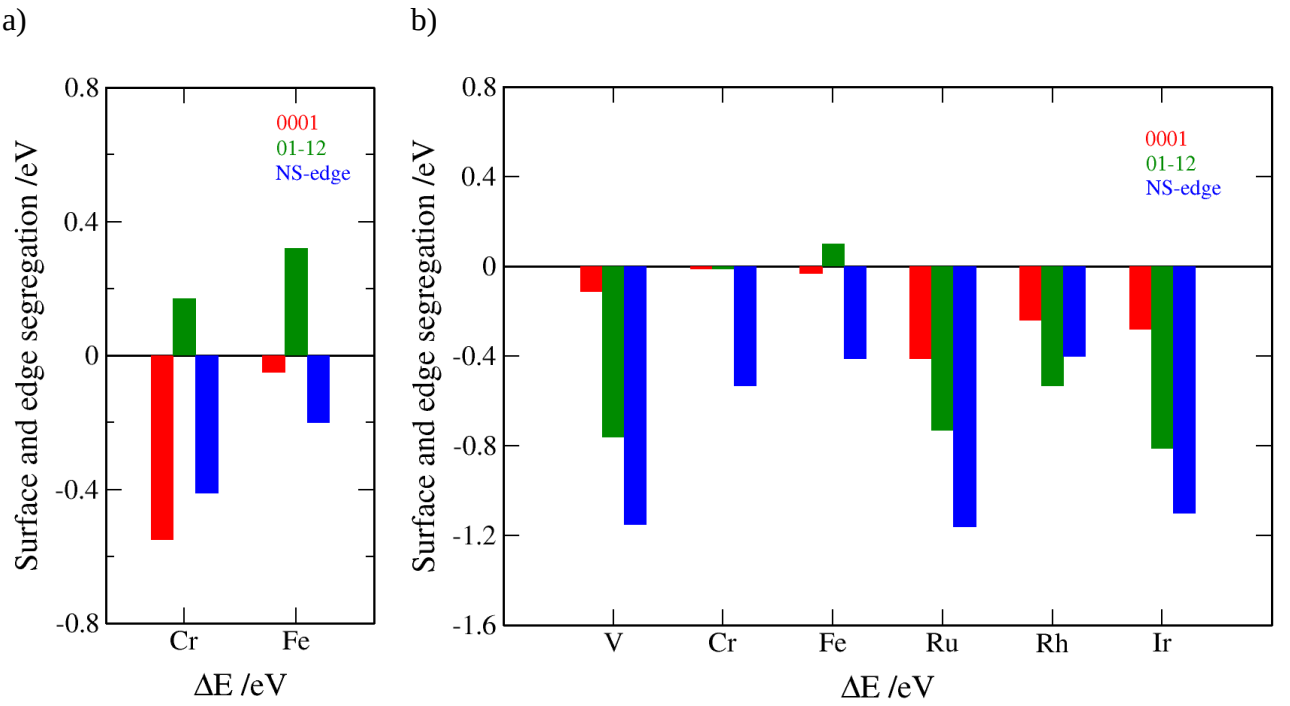

Figure 9 Calculated surface and edge segregation energies for stable doped a) Co and b) Ni oxyhydroxides. Negative values indicate that segregation to the surface/edge is energetically favored.

3.3.2. Catalytic activity

In the following section, we calculate activities for dopants that have a propensity towards surface or edge segregation. For dopants that prefer to remain in the bulk, we do not expect any activity change with respect to pure catalysts. For dopants that prefer NS terraces, the activity has already been reported in Table 1. On most of the stable catalysts, oxygen evolution takes place *via* the 1st reaction mechanism. Exemptions are Cr and Fe doped (0001) surfaces, for which step (9) in the 3rd reaction pathway is the PDS. For Ru and Ir doped (01-12), alternative pathways are much higher in free energy than the 1st reaction mechanism. Free energy values for the different electrochemical steps (1, 2+3, 4, 5 and 9) are tabulated in Note 6 in the ESI.

Table 2 Activities of selected doped Co and Ni ox-hys. Label 'bulk' indicates that dopant prefers the bulk site, meaning that the activity will be the same as on the pure catalyst. The values are given in units of volts.

		Co oxyhydroxide	
	0001	01-12	NS-edge
pristine	0.61	0.81	0.71
Cr	0.64	bulk	0.77
Fe	0.54	bulk	0.70
		Ni oxyhydroxide	
	0001	01-12	NS-edge
pristine	0.60	1.15	0.55
V	0.38	0.66	0.91
Cr	0.49	0.86	0.49
Fe	0.50	bulk	1.04
Ru	0.70	0.70	1.03
Rh	0.49	0.30	0.25
Ir	0.80	0.45	1.10

It is hard to derive a systematic trend from results in Table 2, because activities do not only depend on dopant element, but also on the surface termination The catalyst with the highest reported activity that consistently reduces the overpotential regardless of the surface termination is Rh doped Ni ox-hy. To ascertain this result we have performed HSE calculations on the different terminations of pure and Rh doped NiOOH. Herein, we bring only the most important conclusions, calculation details and other results are presented in Note 9 in the ESI. HSE gives consistently higher reaction overpotentials than DFT+U, but the absolute trend is the same, clearly emphasizing the promoting role of Rh on the NiOOH activity. Both DFT+U and hybrid functionals are approximative methods for taking strong electron correlations into account. For high-accuracy activity assessments, it would be necessary to use a quantum chemical method, such as MP2 (Møller–Plesset second order perturbation theory), CCSD (coupled cluster with single and double excitation) or similar. Applying such high-level methods is not tractable for the bulk terminations due to the large system sizes, but

might be possible for the NS structures. Making a detailed, comparative analysis using different levels of theory is beyond the scope of this study and will be the topic of another publication.

Conclusions

In summary, we have performed a comprehensive and systematic analysis, wherein we have investigated in detail the pure and doped Ni and Co ox-hys going from 3D bulk oxides down to single-layer NS, the effect of terrace and edges and the influence of 25 different dopants on the stability, activity and conductivity at oxygen evolution potentials. The main conclusions are summarized in the following points.

1. From a mechanistic perspective, on all the doped NS and most of the doped bulk and edge terminations, oxygen evolution takes place at a single site.
2. Ni ox-hys are in general more active OER electrocatalysts than their Co ox-hys counterparts, with the exception of the bulk edge.
3. It is more favorable to dope Ni than Co ox-hys, with the most stable dopants being first row transition and noble metals. Doped 2D NS are less stable than doped 3D materials because electrostatic interactions between incorporated metal cations and intercalated anions exert a stabilizing effect on the structure.
4. Electronic conductance is dependent on the nature of the dopant atom and its valence, and might change as a function of potential. We find that at OER potentials, Fe exists as conductive Fe^{4+}.
5. The best catalyst candidates are Fe doped Co, and V, Fe, Ru, Ir and Rh doped Ni ox-hys, where the Rh doped Ni ox-hys stands out as the catalyst with the highest activity.

In this study, we have applied a set of necessary approximations (e.g. assuming specific reaction mechanisms, the electronic Hubbard U correction for explicitly treating the on-site Coulomb interactions etc.) for studying the properties of the ox-hys. We have tried to make our model as realistically as possible, but certain aspects of the environment (e.g. the presence of aqueous electrolyte, explicit description of the potential and electric field in the simulated cell) and the model (the possibility of surface reconstruction, different arrangements of dopant atoms) have not been taken into account explicitly. Including all the details of the solid/liquid interface and describing the electronic structure of complex oxides are fundamental challenges, and before they are resolved, we have to rely on more approximate models and methods.

Supporting Information

Supporting Information contains 7 Notes:

Note 1: Calculation of heats of formation of ion-intercalated electrodes.

Note 2: Preferential arrangement of hydroxyls in oxyhydroxides.

Note 3: Dehydrogenation isotherms for the pristine and doped nanosheets.

Note 4: Electronic structure for bulk oxyhydroxides as a function of U.

Note 5: Tables of reference oxides used to calculate stabilities of doped nanosheets.

Note 6: Tabulated values of reaction overpotentials.

Note 7: DOS plots for doped nanosheets.

Note 8: Segregation directions for dopants at (0001) and (01-12) terminations.

Note 9: HSE calculations for pure and Rh-doped NiOOH.

Contact information

Corresponding author:

Vladimir Tripkovic, email: tripce@gmail.com

Mailing address: Department of Energy Conversion and Storage, Technical University of Denmark, Fysikvej - building 309, 2800 Lyngby, Denmark.

Acknowledgements

This work was supported by the Horizon 2020 framework, grant number 646186. We would also like to acknowledge the Velux Foundations through the research center V-Sustain, grant number 9455.

References

(1) Nørskov, J. K.; Bligaard, T.; Rossmeisl, J.; Christensen, C. H. *Nat. Chem.* **2009**, *1*, 37–46.

(2) Suntivich, J.; May, K. J.; Gasteiger, H. A.; Goodenough, J. B.; Shao-Horn, Y. *Science (80-.).* **2011**, *334*, 1383–1385.

(3) Matsumoto, Y.; Sato, E. *Mater. Chem. Phys.* **1986**, *4*, 397–426.

(4) Valdes, A.; Brillet, J.; Gratzel, M.; Gudmundsdottir, H.; Hansen, H. A.; Jonsson, H.; Klupfel, P.; Kroes, G. J.; Le Formal, F.; Man, I. C.; Martins, R. S.; Norskov, J. K.; Rossmeisl, J.; Sivula, K.; Vojvodic, A.; Zach, M. *Phys. Chem. Chem. Phys.* **2012**, *14*, 49–70.

(5) Man, I. C.; Su, H.-Y.; Calle-Vallejo, F.; Hansen, H. A.; Martínez, J. I.; Inoglu, N. G.; Kitchin, J.; Jaramillo, T. F.; Nørskov, J. K.; Rossmeisl, J. *ChemCatChem* **2011**, *3*, 1159–

1165.

(6) McCrory, C. C. L.; Jung, S.; Peters, J. C.; Jaramillo, T. F. *J. Am. Chem. Soc.* **2013**, *135*, 16977–16987.

(7) Walter, M. G.; Warren, E. L.; McKone, J. R.; Boettcher, S. W.; Mi, Q.; Santori, E. A.; Lewis, N. S. *Chem. Rev.* **2010**, *110*, 6446–6473.

(8) Lee, Y.; Suntivich, J.; May, K. J.; Perry, E. E.; Shao-Horn, Y. *J. Phys. Chem. Lett.* **2012**, *3*, 399–404.

(9) Seitz, L. C.; Dickens, C. F.; Nishio, K.; Hikita, Y.; Montoya, J.; Doyle, A.; Kirk, C.; Vojvodic, A.; Hwang, H. Y.; Norskov, J. K.; Jaramillo, T. F. *Science (80-.).* **2016**, *353*, 1011–1014.

(10) Diaz-Morales, O.; Raaijman, S.; Kortlever, R.; Kooyman, P. J.; Wezendonk, T.; Gascon, J.; Fu, W. T.; Koper, M. T. M. *Nat. Commun.* **2016**, *7*, 12363.

(11) Burke, M. S.; Enman, L. J.; Batchellor, A. S.; Zou, S.; Boettcher, S. W. *Chem. Mater.* **2015**, *27*, 7549–7558.

(12) Suntivich, J.; Gasteiger, H. A.; Yabuuchi, N.; Nakanishi, H.; Goodenough, J. B.; Shao-Horn, Y. *Nat. Chem.* **2011**, *3*, 546–550.

(13) Yang, Y.; Fei, H.; Ruan, G.; Xiang, C.; Tour, J. M. *ACS Nano* **2014**, *8*, 9518–9523.

(14) McCrory, C. C. L.; Jung, S.; Ferrer, I. M.; Chatman, S. M.; Peters, J. C.; Jaramillo, T. F. *J. Am. Chem. Soc.* **2015**, *137*, 4347–4357.

(15) Song, F.; Hu, X. *Nat. Commun.* **2014**, *5*, 4477.

(16) Jung, S.; McCrory, C. C. L.; Ferrer, I. M.; Peters, J. C.; Jaramillo, T. F. *J. Mater. Chem. A* **2016**, *4*, 3068–3076.

(17) Yeo, B. S.; Bell, A. T. *J. Am. Chem. Soc.* **2011**, *133*, 5587–5593.

(18) Cheng, F.; Zhang, T.; Zhang, Y.; Du, J.; Han, X.; Chen, J. *Angew. Chem. Int. Ed. Engl.* **2013**, *52*, 2474–2477.

(19) Huang, J.; Chen, J.; Yao, T.; He, J.; Jiang, S.; Sun, Z.; Liu, Q.; Cheng, W.; Hu, F.; Jiang, Y.; Pan, Z.; Wei, S. *Angew. Chem. Int. Ed. Engl.* **2015**, *54*, 8722–8727.

(20) Wu, J.; Ren, Z.; Du, S.; Kong, L.; Liu, B.; Xi, W.; Zhu, J.; Fu, H. *Nano Res.* **2016**, *9*, 713–725.

(21) Zhang, B.; Zheng, X.; Voznyy, O.; Comin, R.; Bajdich, M.; Garcia-Melchor, M.; Han, L.; Xu, J.; Liu, M.; Zheng, L.; Garcia de Arquer, F. P.; Dinh, C. T.; Fan, F.; Yuan, M.; Yassitepe, E.; Chen, N.; Regier, T.; Liu, P.; Li, Y.; De Luna, P.; Janmohamed, A.; Xin, H. L.; Yang, H.; Vojvodic, A.; Sargent, E. H. *Science (80-.).* **2016**, *352*, 333–337.

(22) Bajdich, M.; García-Mota, M.; Vojvodic, A.; Nørskov, J. K.; Bell, A. T. *J. Am. Chem. Soc.* **2013**, *135*, 13521–13530.

(23) Li, Y.-F.; Selloni, A. *ACS Catal.* **2014**, *4*, 1148–1153.

(24) Oliver-Tolentino, M. A.; Vázquez-Samperio, J.; Manzo-Robledo, A.; González-Huerta, R. de G.; Flores-Moreno, J. L.; Ramírez-Rosales, D.; Guzmán-Vargas, A. *J. Phys. Chem. C* **2014**, *118*, 22432–22438.

(25) Dionigi, F.; Strasser, P. *Adv. Energy Mater.* **2016**, 1600621.

(26) Diaz-Morales, O.; Ledezma-Yanez, I.; Koper, M. T. M.; Calle-Vallejo, F. *ACS Catal.* **2015**, *5*, 5380–5387.

(27) Han, Y.; Liu, Z.-H.; Yang, Z.; Wang, Z.; Tang, X.; Wang, T.; Fan, L.; Ooi, K. *Chem. Mater.* **2008**, *20*, 360–363.

(28) Coronado, E.; Galán-Mascarós, J. R.; Martí-Gastaldo, C.; Ribera, A.; Palacios, E.; Castro, M.; Burriel, R. *Inorg. Chem.* **2008**, *47*, 9103–9110.

(29) Xu, Y.; Hao, Y.; Zhang, G.; Lu, Z.; Han, S.; Li, Y.; Sun, X. *RSC Adv.* **2015**, *5*, 55131–55135.

(30) Abellán, G.; Coronado, E.; Martí-Gastaldo, C.; Waerenborgh, J.; Ribera, A. *Inorg. Chem.* **2013**, *52*, 10147–10157.

(31) Liang, H.; Meng, F.; Cabán-Acevedo, M.; Li, L.; Forticaux, A.; Xiu, L.; Wang, Z.; Jin, S. *Nano Lett.* **2015**, *15*, 1421–1427.

(32) Trotochaud, L.; Ranney, J. K.; Williams, K. N.; Boettcher, S. W. *J. Am. Chem. Soc.* **2012**, *134*, 17253–17261.

(33) Louie, M. W.; Bell, A. T. *J. Am. Chem. Soc.* **2013**, *135*, 12329–12337.

(34) Gong, M.; Dai, H. *Nano Res.* **2015**, *8*, 23–39.

(35) Gerken, J. B.; Shaner, S. E.; Massé, R. C.; Porubsky, N. J.; Stahl, S. S. *Energy Environ. Sci.* **2014**, *7*, 2376–2382.

(36) Gong, M.; Li, Y.; Wang, H.; Liang, Y.; Wu, J. Z.; Zhou, J.; Wang, J.; Regier, T.; Wei, F.; Dai, H. *J. Am. Chem. Soc.* **2013**, *135*, 8452–8455.

(37) Smith, R. D. L.; Prevot, M. S.; Fagan, R. D.; Zhang, Z.; Sedach, P. A.; Siu, M. K. J.; Trudel, S.; Berlinguette, C. P. *Science (80-.).* **2013**, *340*, 60–63.

(38) Corrigan, D. A.; Conell, R. S.; Fierro, C. A.; Scherson, D. A. *J. Phys. Chem* **1987**, *91*, 5009–5011.

(39) Corrigan, D. A. *J. Electrochem. Soc.* **1987**, *134*, 377.

(40) Klaus, S.; Cai, Y.; Louie, M. W.; Trotochaud, L.; Bell, A. T. *J. Phys. Chem. C* **2015**, *119*, 7243–7254.

(41) Burke, M. S.; Kast, M. G.; Trotochaud, L.; Smith, A. M.; Boettcher, S. W. *J. Am. Chem. Soc.* **2015**, *137*, 3638–3648.

(42) Burke, M. S.; Zou, S.; Enman, L. J.; Kellon, J. E.; Gabor, C. A.; Pledger, E.; Boettcher, S. W.

J. Phys. Chem. Lett. **2015**, *6*, 3737–3742.

(43) Hong, D.; Yamada, Y.; Nagatomi, T.; Takai, Y.; Fukuzumi, S. *J. Am. Chem. Soc.* **2012**, *134*, 19572–19575.

(44) Li, Y.-F.; Selloni, A. *ACS Catal.* **2014**, *4*, 1148–1153.

(45) Swierk, J. R.; Klaus, S.; Trotochaud, L.; Bell, A. T.; Tilley, T. D. *J. Phys. Chem. C* **2015**, *119*, 19022–19029.

(46) Trotochaud, L.; Young, S. L.; Ranney, J. K.; Boettcher, S. W. *J. Am. Chem. Soc.* **2014**, *136*, 6744–6753.

(47) Friebel, D.; Louie, M. W.; Bajdich, M.; Sanwald, K. E.; Cai, Y.; Wise, A. M.; Cheng, M.-J.; Sokaras, D.; Weng, T.-C.; Alonso-Mori, R.; Davis, R. C.; Bargar, J. R.; Nørskov, J. K.; Nilsson, A.; Bell, A. T. *J. Am. Chem. Soc.* **2015**, *137*, 1305–1313.

(48) Hammer, B.; Hansen, L.; Nørskov, J. *Phys. Rev. B* **1999**, *59*, 7413–7421.

(49) Dudarev, S. L.; Botton, G. A.; Savrasov, S. Y.; Humphreys, C. J.; Sutton, A. P. *Phys. Rev. B* **1998**, *57*, 1505–1509.

(50) Mortensen, J.; Hansen, L.; Jacobsen, K. *Phys. Rev. B* **2005**, *71*, 1–11.

(51) García-Mota, M.; Bajdich, M.; Viswanathan, V.; Vojvodic, A.; Bell, A. T.; Nørskov, J. K. *J. Phys. Chem. C* **2012**, *116*, 21077–21082.

(52) Chen, J.; Selloni, A. *Phys. Rev. B* **2012**, *85*, 85306.

(53) Cococcioni, M.; de Gironcoli, S. *Phys. Rev. B* **2005**, *71*, 35105.

(54) Chevrier, V. L.; Ong, S. P.; Armiento, R.; Chan, M. K. Y.; Ceder, G. *Phys. Rev. B* **2010**, *82*, 75122.

(55) Heyd, J.; Scuseria, G. E.; Ernzerhof, M. *J. Chem. Phys.* **2003**, *118*, 8207–8215.

(56) Radin, M. D.; Siegel, D. J. *Energy Environ. Sci.* **2013**, *6*, 2370.

(57) Huefner, M.; Ghosh, R. K.; Freeman, E.; Shukla, N.; Paik, H.; Schlom, D. G.; Datta, S. *Nano Lett.* **2014**, *14*, 6115–6120.

(58) Wang, Y.; Fang, H.; Zacherl, C. L.; Mei, Z.; Shang, S.; Chen, L.-Q.; Jablonski, P. D.; Liu, Z.-K. *Surf. Sci.* **2012**, *606*, 1422–1425.

(59) Monkhorst, H. J. *Phys. Rev. B* **1976**, *13*, 5188–5192.

(60) Henkelman, G.; Jónsson, H. *J. Chem. Phys.* **2000**, *113*, 9978.

(61) Henkelman, G.; Uberuaga, B. P.; Jónsson, H. *J. Chem* **2000**, *113*, 9901.

(62) Nørskov, J. K.; Rossmeisl, J.; Logadottir, A.; Lindqvist, L.; Kitchin, J. R.; Bligaard, T.; Jonsson, H. *J. Phys. Chem. B* **2004**, *108*, 17886–17892.

(63) Blöchl, P. E. *Phys. Rev. B* **2000**, *62*, 6158–6179.

(64) Tkalych, A. J.; Yu, K.; Carter, E. A. *J. Phys. Chem. C* **2015**, *119*, 24315–24322.

(65) Pourbaix, M. *Atlas of Electrochemical Equilibria in Aqueous Solutions*, Second.; National Association of Corrosion Engineers: Houston, Texas, 1974.

(66) Bediako, D. K.; Lassalle-Kaiser, B.; Surendranath, Y.; Yano, J.; Yachandra, V. K.; Nocera, D. G. *J. Am. Chem. Soc.* **2012**, *134*, 6801–6809.

(67) McAlpin, J. G.; Surendranath, Y.; Dinca, M.; Stich, T. A.; Stoian, S. A.; Casey, W. H.; Nocera, D. G.; Britt, R. D. *J. Am. Chem. Soc.* **2010**, *132*, 6882–6883.

(68) Desilvestro, J.; Corrigan, D. A.; Weaver, M. J. *J. Phys. Chem.* **1986**, *90*, 6408–6411.

(69) Axmann, P.; Glemser, O. *J. Alloys Compd.* **1997**, *246*, 232–241.

(70) Ng, J. W. D.; García-Melchor, M.; Bajdich, M.; Chakthranont, P.; Kirk, C.; Vojvodic, A.; Jaramillo, T. F. *Nat. Energy* **2016**, *1*, 16053.

(71) Görlin, M.; Chernev, P.; Ferreira de Araújo, J.; Reier, T.; Dresp, S.; Paul, B.; Krähnert, R.; Dau, H.; Strasser, P. *J. Am. Chem. Soc.* **2016**, *138*, 5603–5614.

(72) Stamenkovic, V. R.; Fowler, B.; Mun, B. S.; Wang, G. F.; Ross, P. N.; Lucas, C. A.; Markovic, N. M. *Science (80-.).* **2007**, *315*, 493–497.

(73) Lyons, M. E. G.; Brandon, M. P. *J. Electroanal. Chem.* **2010**, *641*, 119–130.

(74) Tripkovic, V.; Skúlason, E.; Siahrostami, S.; Nørskov, J. K.; Rossmeisl, J. *Electrochim. Acta* **2010**, *55*, 7975–7981.

(75) Calle-Vallejo, F.; Díaz-Morales, O. A.; Kolb, M. J.; Koper, M. T. M. *ACS Catal.* **2015**, *5*, 869–873.

(76) He, S.; Huang, Y.; Huang, J.; Liu, W.; Yao, T.; Jiang, S.; Tang, F.; Liu, J.; Hu, F.; Pan, Z.; Liu, Q. *J. Phys. Chem. C* **2015**, *119*, 26362–26366.

(77) Gurevich, Y. Y.; Pleskov, Y. V. *Semicond. Semimetals* **1983**, *19*, 255–328.

(78) Younesi, R.; Christiansen, A.; Loftager, S.; García-Lastra, J. M.; Vegge, T.; Norby, P.; Holtappels, P. *ChemSusChem* **2015**, *8*, 3213–3216.

(79) Han, B.; Risch, M.; Lee, Y.-L.; Ling, C.; Jia, H.; Shao-Horn, Y. *Phys. Chem. Chem. Phys.* **2015**, *17*, 22576–22580.

Graphical TOC